Proceedings World Geothermal Congress 2020+1
Reykjavik, Iceland, April - October 2021

Use of Resource Estimation Tools to Refine 3D Earth Model of the Silangkitang Geothermal Field, North Sumatra, Indonesia

Drestanta Yudha Satya, Andrew McMahon, Iain Levy and Doddy Astra

The Energy Building 7th Floor, SCBD Lot 11A, Jl. Jend. Sudirman Kav. 52-53, Jakarta 12190, Indonesia

drestanta.yudha@sarulla-geothermal.com, andrew.mcmahon@seequent.com, iain.levy@seequent.com, doddy.astra@sarulla-geothermal.com

Keywords: Sarulla, Silangkitang, Great Sumatra Fault, 3D earth model

ABSTRACT

As part of the field development plan, the Silangkitang (SIL) 3D earth model has been continuously updated by integrating multidisciplinary (geology, geophysics, geochemistry and reservoir engineering) data and interpretations to produce an accurate geothermal conceptual model. Most resource estimates are undertaken using computer-based block modelling methods utilising 3D block models based on a geological earth model of the resource. For these block models to be valid, it is important that they are constrained by the controlling elements of the resource such as major structural boundaries, lithological changes within rock units, hydrothermal alteration type, compaction effect with depth, and proposed fluid pathways. Extreme heterogeneity in volcanic lithology is one of the challenges of modelling geothermal reservoirs Linked to multiple sources of volcanic products in a geothermal prospect. Furthermore, in the reservoir zone, lithology can be difficult to recognize since mud circulation is normally lost and there and no rock cuttings recovered at the surface. As it is not straightforward to accurately distribute reservoir and rock properties between wells due to the limited spatial distribution, the geologist then undertakes statistical and variogram analysis to give a measure of the spatial distribution of rock and resource properties for the field. An example of where this application becomes powerful in geothermal development is for distributing key reservoir parameters for flow simulation across different formations or 'rock types' when moving from the conceptual model to the flow simulation model. This is often achieved by giving different geological formations or rock types a bulk value for parameters such as porosity and permeability as examples. Normally this is based on analogues and/or multiple models run with different valuesThis paper highlights a workflow where geothermal conceptual model understanding, and statistical methodology are used to populate rock properties from downhole measurements for flow simulation and its impact on the history matching process. It also gives feedback on how this process might inform concepts within the conceptual model.

1. INTRODUCTION

The Silangkitang (SIL) Geothermal Field is located in the Tapanuli Utara District, North Sumatra Province, Indonesia. The field is located approximately 35 kilometers southeast of the town of Tarutung. Silangkitang is one of several prospects in the Sarulla contract area (Figure 1).

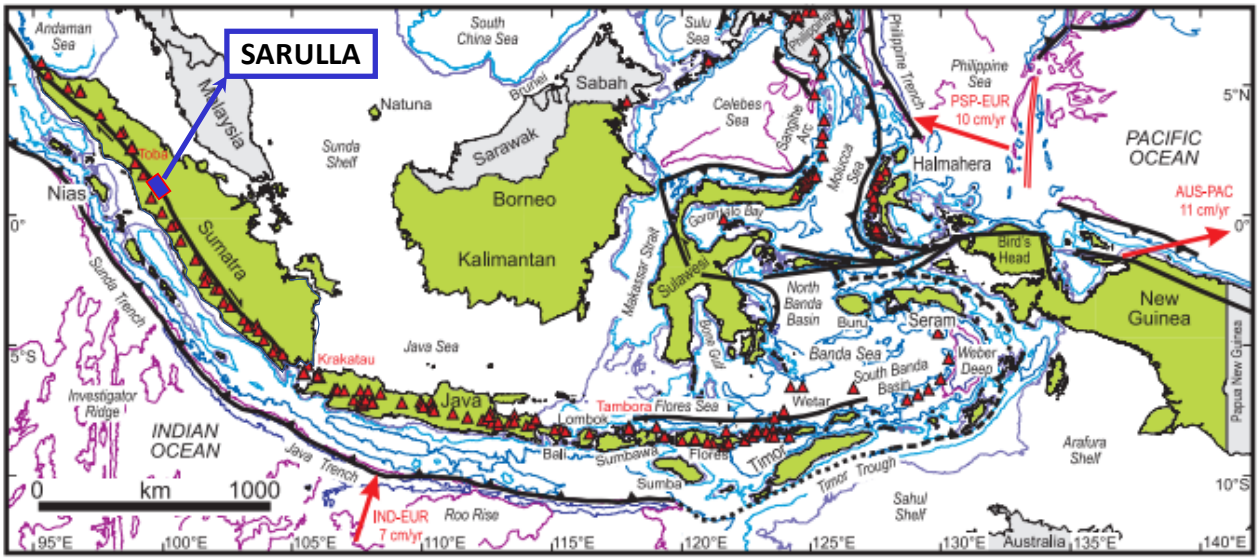

Figure 1: Tectonic map of Indonesia (Hall, 2009), showing the location of Sarulla contract area along Great Sumatra Fault Zone (GSFZ).

Sarulla Operation Limited (SOL), a consortium ofMedco Energi Internasional Tbk, Itochu Corporation, Kyushu Electric Power Co. Inc., Ormat Technologies, Inc., and INPEX Corporation, has been granted the right to utilize the Sarulla geothermal resource for power generation under the framework of a Joint Operating Contract (JOC) with Pertamina. SIL started commercial generation of

110 MW on Mar 18, 2017. Currently SOL has 3 units commercially running at Namora-I-Langit (220 MW) and Silangkitang (110 MW) under a single contract. At SIL there are 4 production wells and 9 injection wells to support full power generation.

2. GEOLOGICAL SETTING

The SIL field is situated within the Sunda volcanic arc which is structurally uplifted and covered by young volcanic rocks. During the Miocene epoch, the right lateral Great Sumatra Fault Zone (GSFZ) is interpreted to accommodate the oblique subduction which slips at a rate of around 23 ± 2 mm/year nearby Lake Toba in northern Sumatra (Bellier and Sebrier, 1995) to 25 mm/year based on geodetic measurement (Genrich at al., 2000). Although there are no active volcanoes positioned in the Sarulla district, there are volcanic eruptive centers less than million years old located within and close to the contract area.

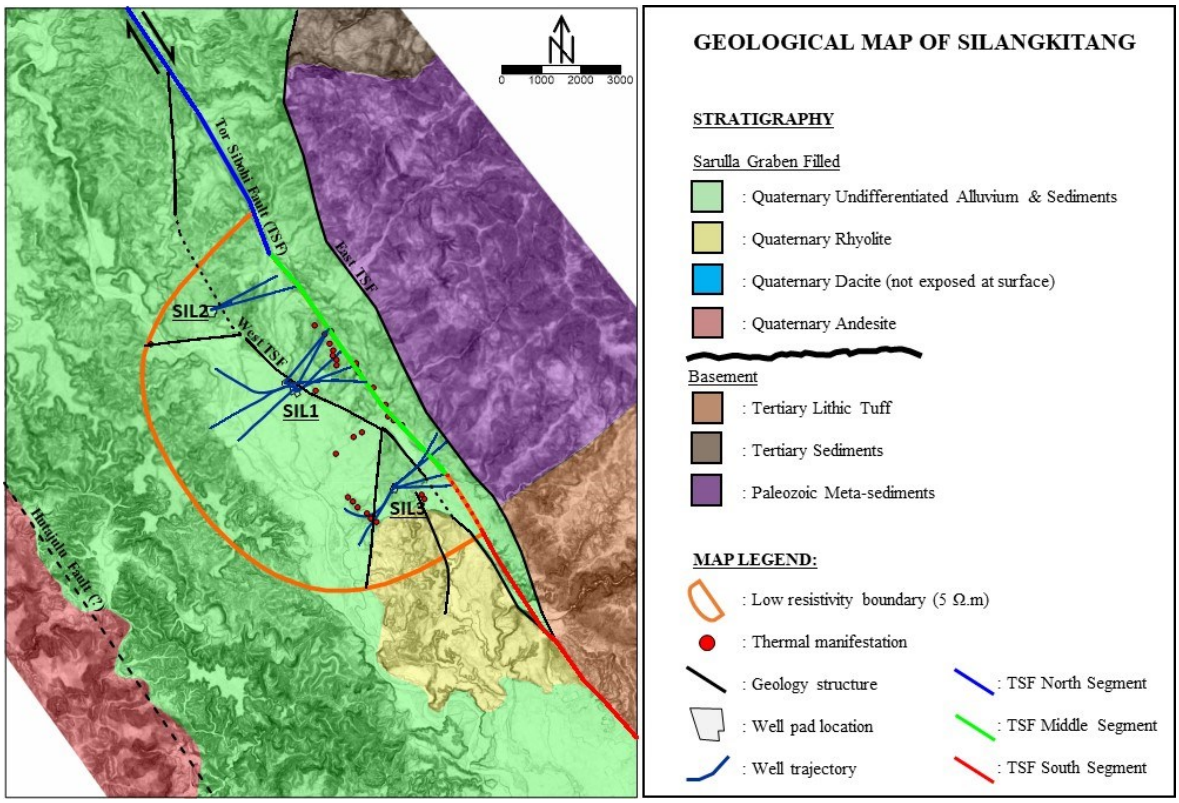

Figure 2: Surface geologic map of the Silangkitang area with major rock types and prominent faults. The low resistivity boundary (defined from MT surveys), well locations, and thermal manifestations are also indicated.

The main surface expression of the SIL hydrothermal system is comprised of a series of boiling springs and fumaroles, concentrated along a 2-km length of the GSFZ. The geochemistry and geophysical surveys indicate a high temperature geothermal system and local less resistive layer that coincides with elevated temperature and shallow smectite-rich alteration, respectively. Aspden et al. (1982) and Gunderson et al. (1995, 2000) depicted the Quaternary arc volcanism products which includes widespread Young Toba Tuffs originating from Lake Toba caldera dominated the surface geology. Underneath these dacite-rhyolite volcanic complexes are faulted and folded Paleozoic and Tertiary metasedimentary rock and Mesozoic to Tertiary intrusive rocks (Figure 2).

3. CONCEPTUAL MODEL

The Great Sumatra Fault system is the main structure controlling permeability for the SIL geothermal system. It allows the high temperature source to heat the system and geothermal fluid to move from high to low pressure regions beneath the low resistivity layer. The commercial Silangkitang reservoir is a high temperature (535 – 590ºF) geothermal resource. According to Simatupang (2017), geochemistry analysis using newly drilled well data show liquids are in full equilibrium with observed high temperatures in SIL1 wells that were drilled to the east (Figure 3). The temperature logs also demonstrate that upflow into the reservoir occurs at or near the subsurface location of the NW-bearing SIL1 pad.

Both production and injection wells that penetrated the GSFZ obtained good permeability while other wells drilled to the west encountered lower permeability. The wells at SIL1 and SIL2 have better permeability compared with the wells at SIL3. Detailed mapping along the surface trace of the GSFZ identified releasing bends and fault steps which indicate zones of dilation and correlate with the main upflow zone in the area to the NE & E of SIL1 Pad. The hot geothermal fluid seems to move upward along the highly permeable Tor Sibohi Fault (TSF) and enters into the horizontal aquifer which is the principal outflow for the SIL system. The hot fluid in the geothermal reservoir originates from a deep level at a location close to the SIL1 pad. Based on measured downhole temperatures, ascending fluids flow at least as far as the SIL2 and SIL3 pads which are located NW and SE of the SIL core area, respectively. Fluid within the main reservoir migrates under the low-permeability clay-rich layer, based on the relatively high temperatures observed there. Some fluids move further up the fault and feed the many thermal features (fumaroles and springs) at the surface (Figure 3).

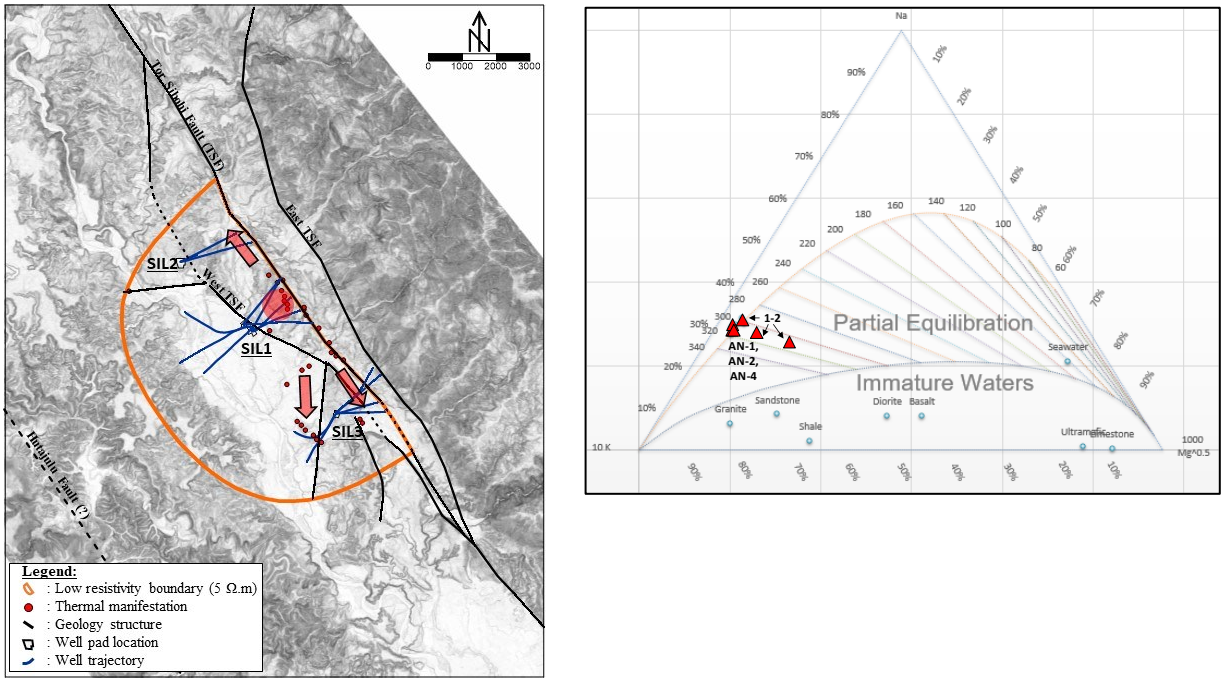

Figure 3: Map view of the SIL conceptual model. Upflow is indicated by red circle and outflow by the red arrows (left). The Na-K-Mg Giggenbach Ternary of wells at Pad-A -SIL1 (Simatupang, 2017) (right).

4. PREVIOUS 3D EARTH MODEL

The initial 3D geological model was produced in 2018 using Leapfrog Geothermal version 3.5.3. The conceptual model of the SIL geothermal system is well represented by the 3D earth model. In areas where there are no well data, the conceptual model was primarily adopted to distribute the reservoir properties. Major structures that play an important role to SIL subsurface geology conditions include two NW-SE orientated faults within the GSFZ and several N-S striking faults near the SIL2 location (Figure 4). These major faults within the GSFZ were incorporated into the geology model to constrain offset stratigraphy layers. One of the SIL wells penetrated completely through the GSFZ and encountered Paleozoic meta-argillite basement at depth on the eastern side of GSFZ. There is shallow basement rock along the eastern portion of the GSFZ as compared with the basement on the western side and the two faults have nearly vertical dip angles. Since there is no well which intersects the Paleozoic Meta-sediments west of the GSFZ, the gravity interpretations were integrated as a constraint to better represent the basement rock in the model. The modelled surface interpreted from gravity data is used as an indicator of the basement depth, at regional scale, and affords useful guidelines where there are no surface or downhole data. In facies modelling the gravity model was also used as a reference to distribute Tertiary Sediment facies where there are no well data. Gravity data shows basement highs at both west and east boundaries of the graben, so the Tertiary Sediment formation is interpreted thinning at these graben boundaries. In the model, Quaternary volcanic formations were created using lithology information from drilling (Figure 4).

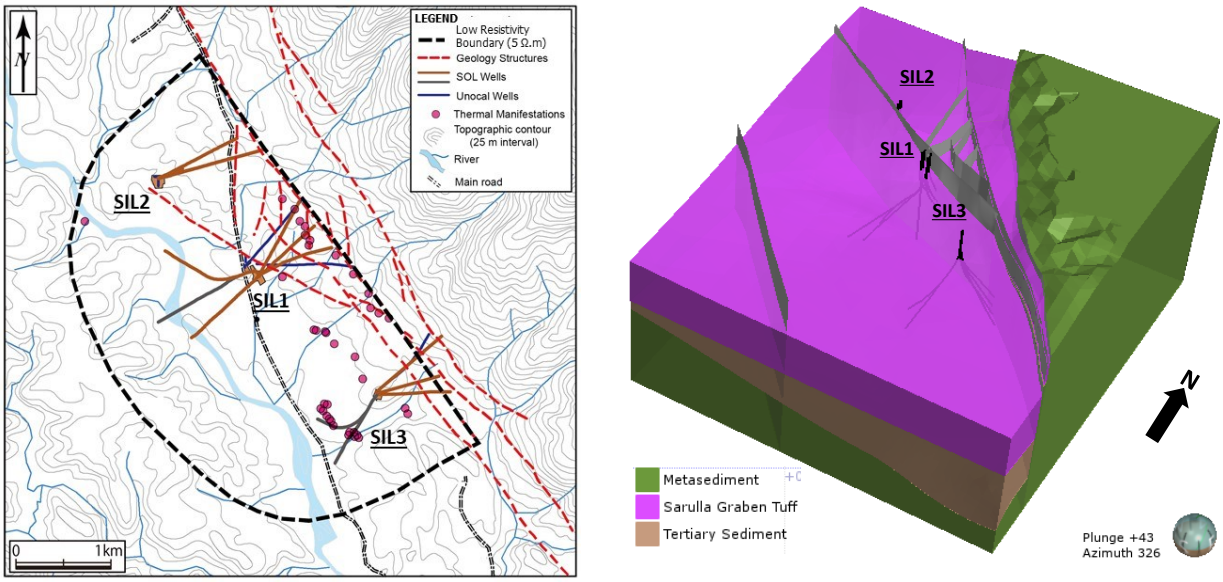

Figure 4: Map showing interpreted structures that are used in the previous static model (left). Snapshot of the 3D visualization of geological model. The stratigraphy offsets are controlled by the main structures within GSFZ (right).

An earth model is the framework to support a realistic numerical model grid (Satya et al., 2018). An earth model can provide general values of several reservoir properties according to the distribution of lithology or rock facies and hydrothermal alteration. In the model, the reservoir properties such as porosity, permeability, conductivity, specific heat, etc. were generally assigned according to rock or formation type. The porosity value is based on the average value of direct measurement from 127 core samples in SIL. The SIL numerical model generalized porosity distribution by using constant values for entire reservoir rocks, and in particular no depth dependency is assumed, in spite of the relatively deep position of the reservoir bottom. This might be optimistic, as it is generally known that porosity tends to decrease with depth.

5. THE 3D EARTH MODEL REFINEMENT

Recent studies at SIL concluded the high permeability zone was restricted within GSFZ, although the low resistivity extends west of the sweet spot area. Definition of lateral and vertical reservoir boundary within modelling activity was also introduced to reveal better understanding about SIL resource area.

5.1 Updated Geological Structures

The geology, geochemistry, geophysics, and reservoir engineering data were used to define important subsurface structures at SIL. Within the SIL area, two main strands of GSF were identified at the east and west boundaries of the Sarulla Graben (Figure 5). The major dextral strike-slip strand of the GSF system, the Tor Sibohi Fault (TSF), is easily observable as a NW-trending break in slope with dextral offsets in streams (e.g., Hickman et al., 2004). This main fault, as suggested by topography, river offsets and the nature of fault development outlines an open constraining bend.

The GSF strand, parallel to the TSF main fault, is bounded the Sarulla graben with Paleozoic meta-sediment basement at the eastern portion. This fault is referred to as the East Tor Sibohi fault (ETSF). Graben filled deposits such as alluvium, lake sediments, and Quaternary volcanic rocks were interpreted as thin layers within the block between main TSF and ETSF strand. This was also where the basement was encountered at shallow depth and interpreted as a result of uplifting along Barisan Mountain.

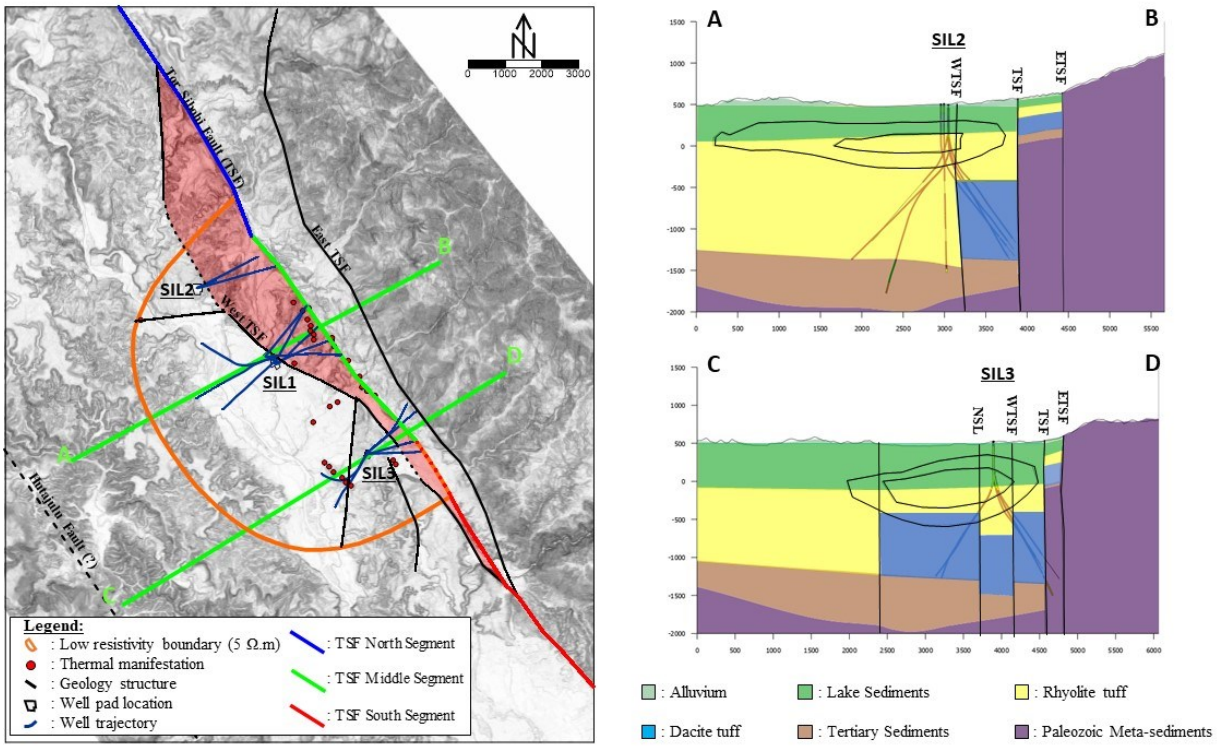

Figure 5: Satellite imagery with prominent geology structures and two NE-SW geology cross sections. Four main structures striking NW-SE are the Tor Sibohi Fault (TSF), East Tor Sibohi Fault (TSF), West Tor Sibohi Fault (WTSF), and Hutajulu Fault. Three minor structures linked to the main structure are located west of WTSF. Low resistivity boundary, well locations, and thermal manifestation. Two NE-SW vertical sections crossing SIL2 and SIL3 show lithostratigraphy and low resistivity contours (small is below 2 ohm while big is below 5 ohm).

Another important lineament, called the West TSF (WTSF), was interpreted to the west of the main TSF which has a variety of strike and seems to be separated from the principal strain in the northern area. This is where a N-S narrow valley can be found, and it joins again 3 km southeast from south most bicarbonate springs. On the map view, it can be clearly seen that WTSF and main TSF create a lens zone where fumaroles nearby SIL1 pad were exposed and the shape of this area becomes narrow at the southern area of SIL (Figure 5). All production wells and most of the injection wells have been drilled within this sweet spot area.

Two N-S lineaments in the vicinity of SIL3 pad were defined as conduits for hot geothermal fluid to reach the surface. One N-S fault showed a horse tail pattern and may contribute to the occurrence of bicarbonate spring in the valley. Other lineaments extended N-S from WTSF along two separated hills and a minor NW structure may allow hot fluid to manifest as NW-oriented bicarbonate. Two

well penetrations were executed to target this specific structure to obtain injection capacity with low pressure interference to the main production wells. Drilling results showed this fault caused depth offset in dacite tuff (Figure 5). Other minor faults striking EW and NE were interpreted as a pathway for geothermal fluid outflowing to west from the system.

5.2 Reservoir Boundary

Based on parameters such as lithology and stratigraphy, hydrothermal alteration, and temperature, the SIL reservoir container was determined. Defining the top of reservoir involves analysis of well observations (i.e. pressure, temperature, permeable zone locations) and other geological (i.e. hydrothermal alterations, Methylene Blue value), and geophysical (i.e. magneto-tellurics and Bouguer gravity) data. The SIL reservoir container has temperature >450°F, commercial permeability as defined by a convective temperature profile, and the presence of the propylitic zone, below the interpreted argillic alteration interval. Based on rock description, the enhanced clay layer associates with the conductive layer of 5 ohm-meter and is considered a clay cap or caprock. Largely, the shallow low resistivity body covers the graben filling rock, capping the reservoir section where most of the production and re-injection wells tap permeability. The eastern boundary of SIL reservoir is NW-SE TSF which is intersected by some wells including newly drilled wells. These have confirmed a major offset of basement rocks across this main fault. The west reservoir edge is principally determined by extrapolated temperature from existing wells and lateral and vertical distribution of base conductor determined from magneto-telluric. The new production and injection wells that penetrated the area between WTSF and TSF obtained good permeability while other wells drilled to the west encountered lower permeability.

6. THE POROSITY WORKFLOW USING ESTIMATION TOOLS

The study focused on updating the 3D SIL earth model, specifically to rationalize reservoir property distribution i.e. porosity using the estimation module within Leapfrog Geothermal version 3.9. The idea to produce a porosity model from the study in Namora-I-Langit, the nearest developed geothermal field in the Sarulla region. There is a need to improve the numerical model by adopting a more realistic porosity distribution which is also geologically reasonable based on previous studies. The porosity properties in the dynamic model are developed by assigning general constant value over the whole reservoir zone with no depth and facies dependency. Again, this might be either optimistic or pessimistic relatives to actual porosity trend that was observed within the reservoir. Therefore, a pilot study was conducted to construct new facies and porosity based on recent study results.

6.1 Porosity Data and Analysis

Porosity measurements were made on representative plug samples taken every 50 feet from cored intervals of the four SIL wells. The highest matrix porosity at >20% were observed from rhyolitic tuff while the argillite has the lowest matrix porosity at <1%. The lava flows and sediment rock have about 12% and 8% average matrix porosity, respectively (Figure 6). Fine-grained pyroclastic has 8% average matrix porosity. About 75% of the data is located within Sarulla Graben Tuff, while 25% of data is within Tertiary Sediment and Metasediment formation.

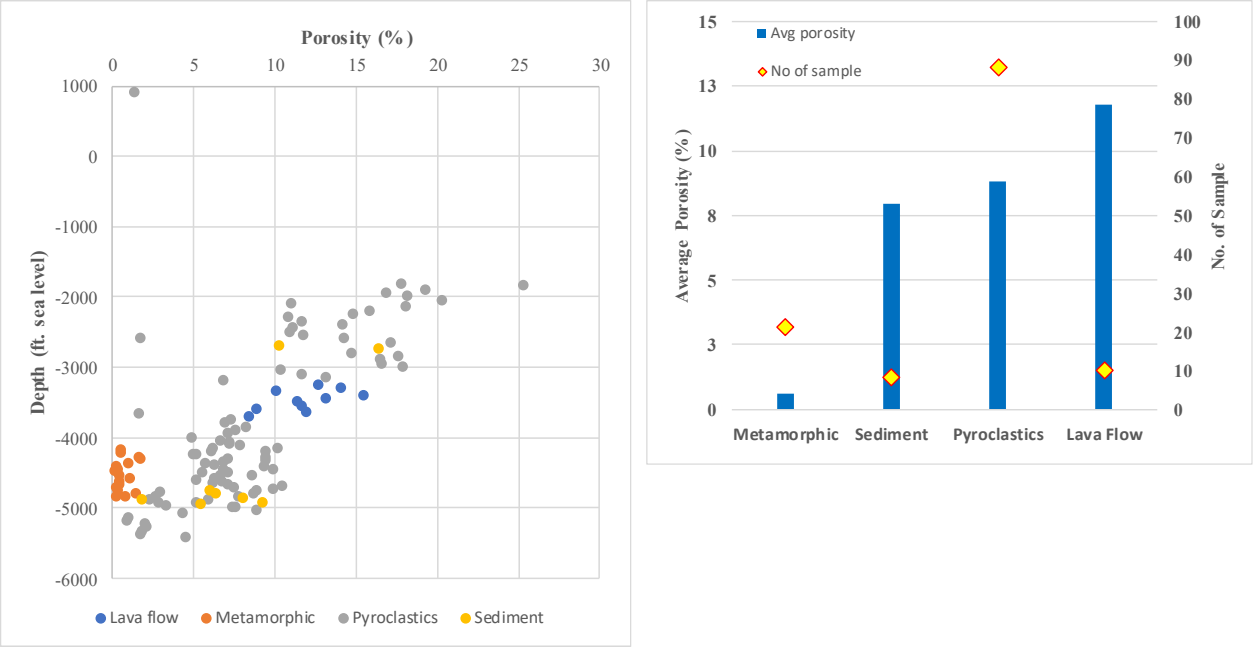

Figure 6: Chart showing matrix porosity vs. depth of the four Lithology Group (LG) at SIL (left). Chart showing the summary of average matrix porosity for each LG in SIL (right).

A previous study concluded that the porosity generally decreases with depth away from the GSFZ (Figure 6). However, porosity may be constant within the fault zone itself (Unocal North Sumatra Geothermal, Ltd., 1996). Matrix porosity at SIL is dependent upon a variety of primary and secondary features including rock type, rock texture and both degree and style of hydrothermal alteration. Paleozoic meta-argillites from SIL3 which drilled to NW have significantly lower porosities (avg. = 0.7%) than the ash-flow tuffs intersected in the other wells. In the SIL1vertical well, porosities of 10-20% (avg. = 14.6%) were measured at subsea depths of 2,000 to 3,000 feet, while lower values of 2-10 % (avg. = 6.5%) were observed at 4,000 to 5,000 feet subsea. Highly altered ash flow tuffs in the SIL2 vertical well have higher porosities than neighboring tuffs that are less strongly altered. Formation of secondary calcite,

quartz, and illite maybe the cause a reduction in porosity in this well. Enhanced porosity was observed in the reservoir section of the SIL1well that was drilled to west in zones where dissolution of minerals occurred.

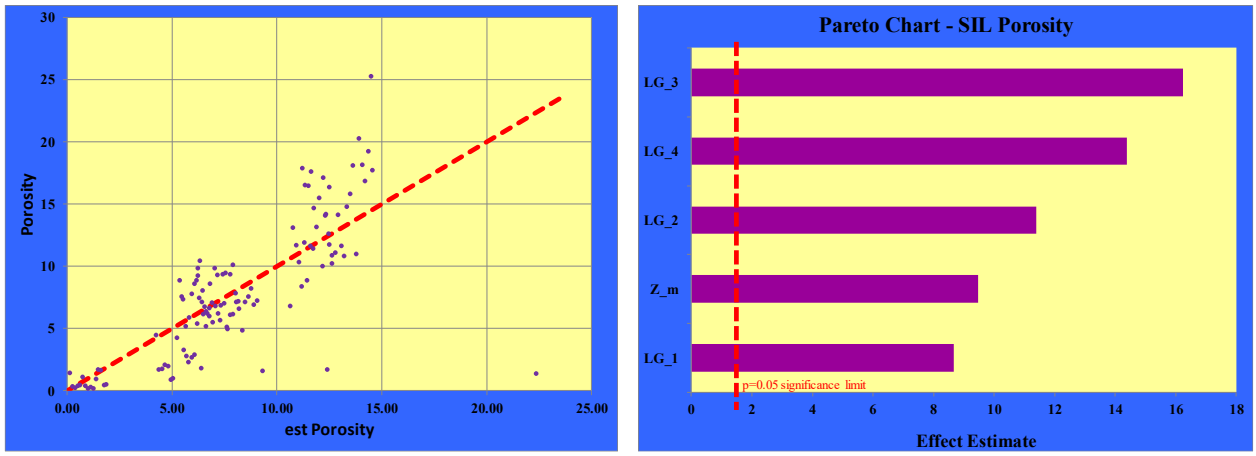

Figure 7: Chart showing relationship between porosity data and estimated porosity that was calculated using defined regression linear function (left). Pareto charts of matrix porosity regression show a statistically-significant correlation with depth and LG (right).

In the recent study, a total of 127 measurements were categorized in four different Lithology Groups (LG) which are metamorphosed sediment rock, fine – coarse grain sedimentary rock, rhyolitic – dacitic pyroclastic rock, and rhyolite. The criteria for the grouping are depositional style and distribution, petrophysical property differences, and lithology type. The trend of decreasing porosity with depth is discernible inside the reservoir and lithology is an important factor that controls the porosity value. A similar trend of decreasing porosities with depth was also observed in the nearby Namora-I-Langit field, where porosity measurements were conducted on 25 core samples from 3 wells. Other geothermal fields such as Darajat, Salak, and Tiwi also show similar porosity characteristic within the reservoir (Aprilina et al., 2015).

For modelling purposes, the probability of each LG was calculated in the entire reservoir section. Based on regression analysis, rock type such as the pyroclastic rocks (LG-3), that dominated the SIL reservoir at depth, show significant correlation with porosity value (Figure 7). This is similar to what was found at the Salak field (Aprilina et al., 2015). A linear equation was determined to explain porosity value in SIL which consists of regression weights for rocks and depth. The function is shown as below:

$$\text{Matrix Porosity} = a*Z + (b*\text{Prob. of LG-1}) + (c*\text{Prob. of LG-2}) + (d*\text{Prob. of LG-3}) + (e*\text{Prob. of LG-4}) \quad (1)$$

where: a, b, c, d, and e are linear regression weights.
Prob. of LG-# is LG indicator probability; and
Z is depth in feet elevation;

6.2 Facies Model

An effort to populate the facies is performed based on an estimated probability of occurrence for each facies within a given lithology. Each facies is given an indicator of either 1 or 0 for where it occurs or does not respectively. These indicators were then upscaled to 10 m intervals to give consistent spacing data downhole. This important step was not done within the estimator itself since then the composite would cross LG facies making composites that are not 0 or 1. Both Kriging (Kr) and Inverse Distance (ID) methods were applied to distribute the probability of each facies at a single point within the reservoir container.

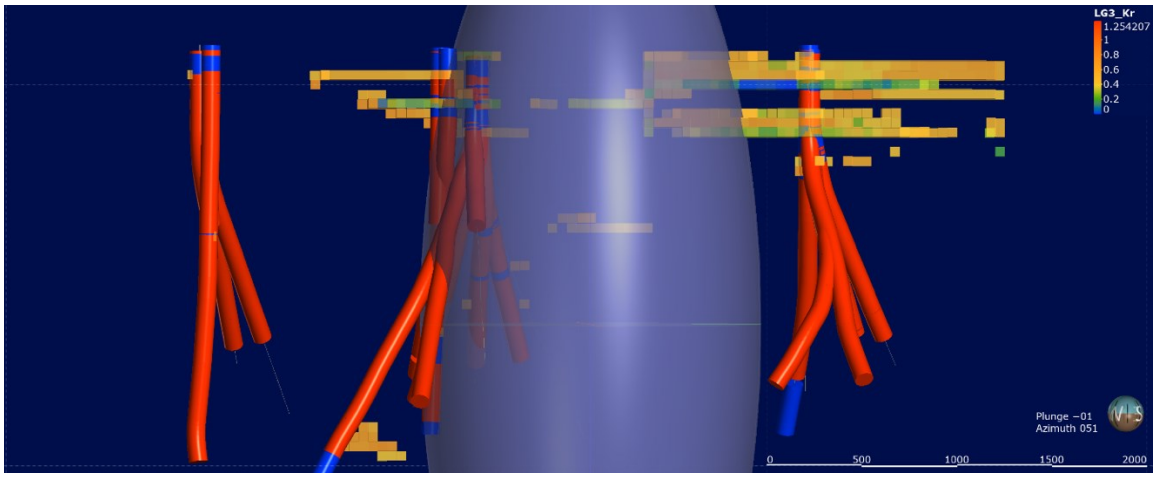

Figure 8: The N-S section showing Kr result of LG-3. Ellipsoid represents variogram that skewed in Z direction to honor the data.

Kr uses a variogram based on the correlation of data at various distances to assign weighting to the samples, while for the ID estimates, the power was set to 2 as a standard value for ID estimation. For each estimator, a search ellipse of 1000, 1000, 200 was selected to reflect the narrow horizontal distribution of the facies, and there was sample size limit to use between 2-30 samples. (Figure 8). Some of the lithology domains did not produce robust variograms and others created unrealistic continuity in the z direction. Without robust variograms, using Kr loses some of its perceived advantages as an estimator over ID. As a check of the performance of the estimators, each block was assigned the facies with the highest probability to create a discrete facies model. This was compared against an implicit model of the facies to confirm that they were similar. Since each lithology probability is calculated independent of the other lithologies, the sum of the 4 facies probabilities is not always equal 1. Normalization of probabilities was completed by dividing the predicted probability by the sum of probabilities for each of the facies.

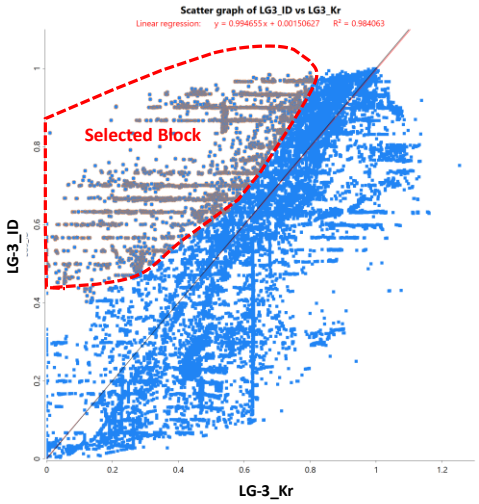

Figure 9: Scatter graph showing Kr vs. ID of the LG-3 probability result at SIL.

Looking at the performance between the ID vs Kr probabilities, it can be seen that while there is some spread, they do have a strong correlation. As shown by "selected block" of LG-3 in (Figure 9), the ID is giving higher probability that Kr estimate (~0.9 vs. 0.5) in the area of the domain that has the lithological complexity. The Kr estimator is smearing the probabilities in the Z plane effectively averaging the area and trending toward the center probability of 0.5. The reason for this is because most of the domain is a single lithology (LG-3) and so in the Z direction, the correlation is skewed and smears the probabilities estimated into this area to trend towards a 50/50 situation resulting in the variogram within LG-3 being skewed in the Z direction. The ID is honoring the horizontal trend better and defining stronger probabilities for each lens. With ID, since the correlation is linked to the search ellipse which can be controlled, this search ellipse should reflect the geological interpretation. The Kr result in this case gives a more globally accurate account while the ID provides a more localized accuracy.

6.2 Porosity Model

The matrix porosity in the SIL static model was distributed laterally using both Kr and ID per LG while for the vertical distribution, the facies model coupled with regression weights for rocks were applied using Equation-1. The normalized probabilities were used in this equation for porosity. The calculated porosity from both Kr and ID shows that the trend of decreasing porosity with depth is aligned with the observation on porosity measurement from core plugs. As shown in Figure 9 there is very good correlation with some spreads when the probabilities are not normalized. There is less correlation where the sum of probabilities is below 0.7 or above 1.2. However, once the probabilities are normalized there is almost no difference between the Kr and ID outputs so either can reflect the porosity trend in SIL and be effectively used (Figure 10).

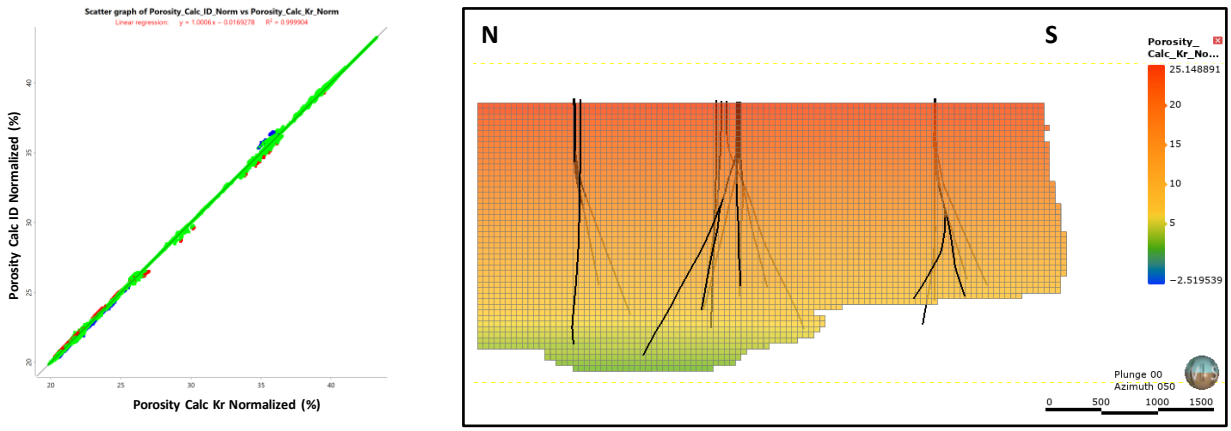

Figure 10: The graph showing relationship porosity that was calculated from Kr and ID (left). N-S cross section showing calculated porosity from Kr LG probability. The global trend of porosity decreasing with depth is well represented.

Based on the estimated values, there were negative porosity values observed in the deeper section of the reservoir which is associated with the depth of interpreted basement based on gravity data. Whereas the high porosity occurs right below the interpreted clay cap that has less influence of compaction but has more intensive alteration. With current assumption on lateral correlation, the high porosity area is located adjacent to vicinity of GSFZ where both producers and injectors found good result in the SIL sweet spot area.

7. DISCUSSION

Recent static modelling work in SIL resulted in new porosity models that honor general trends that decreases with depth away from the GSFZ and are dependent upon a variety of primary and secondary features. This includes rock type, rock texture and both degree and style of hydrothermal alteration. The current workflow provides promising results and as new data are collected this workflow would allow us to update the existing model. The next step would be to apply this workflow to other reservoir properties e.g. temperature, permeability, etc. The results will improve the numerical modelling process such as history matching and forecasting. The flexibility of the new Estimator Tools in Leapfrog Geothermal allows the modeler to visualize the reservoir parameter that is geologically reasonable and also fulfills the geostatistics concept.

ACKNOWLEDMENT

The authors would like to show our gratitude to Sarulla Operations Limited (SOL), sponsor companies through representative Board of Directors of Itochu Corporation, Kyushu Electric Power Co Inc., Medco Energy International Tbk., Inpex Corporation, and Ormat Technologies, and Pertamina Geothermal Energy (PGE) for supporting this project and granting permission to publish this paper. Also, this project could not have been undertaken without the support and encouragement of Seequent Limited.

REFERENCES

Aprilina, N.V., Satya, D.Y., Rejeki. S., Golla, G., and Waite, M.: Geologic Modelling Workflow for Volcanic Hosted Geothermal Reservoirs: Case Study from Salak Geothermal Field, *Proceedings*, World Geothermal Congress, (2015).

Aspden, J.A., Kartawa, W., Aldiss, D.T., Djunuddin, A., Diatma, D., Clarke, M.C.G., Whandoyo, R., and Harahap, H.: Geological Map of the Padangsidempuan and Sibolga Quadrangles, Sumatra, Pusat Penelitian dan Pengembangan Geologi, Bandung, (1982).

Bellier, O., Se´brier, M.: Is The Slip Rate Variation on The Great Sumatra Fault Accommodated by Fore-Arc Stretching?, Geophysical Research Letters, **22**, (1995), 1969–1972.

Genrich, J.F., Bock, Y., McCaffrey, R., Prawirodirdjo, L., Stevens, C.W., Puntodewo, S.S.O., Subarya, C., Wdowinski, S.: Distribution of Slip at The Northern Sumatra Fault System, Journal of Geophysical Research 105, **28**, (2000), 327-328.

Gunderson, R.P., Dobson, P.F., Sharp, W.D., Pudjianto, R., and Hasibuan, A.: Geology and Thermal Features of the Sarulla Contract Area, North Sumatra, Indonesia, *Proceedings*, World Geothermal Congress, (1995), 687-692.

Gunderson, R., Ganefianto, N., Riedel, K., Sirad-Azwar, L., and Suleiman, S.: Exploration Results in The Sarulla Block, North Sumatra, Indonesia, *Proceedings*, World Geothermal Congress, (2000), 1183-1188.

Hall, R.: Indonesia, Geology, *Encyclopedia of Islands*, Univ. California Press, Berkley, California, (2009), 454-460.

Hickman, R.G., Dobson, P.F., van Gerven, M., Sagala, B.D., and Gunderson, R.P.: Tectonic and Stratigraphic Evolution of the Sarulla Graben Geothermal Area, North Sumatra, Indonesia, Journal of Asian Earth Sciences, **23**, (2004), 435448.

Satya, D.Y., Soeda, Y., Drakos, P., Astra, D., Lobato, E. M. L.: Building A 3D Earth Model of Silangkitang Geothermal Field, North Sumatra, Indonesia, Proceedings of the 6th Indonesia International Geothermal Convention & Exhibition, (2018).

Simatupang, C.: Silangkitang Conceptual Model with Newly Drilled Well Based on Geochemistry Interpretation, Unpublished SOL Presentation, (2017).

Unocal North Sumatra Geothermal, Ltd.: Silangkitang Project Resource Feasibility Study, Unpublished Unocal Report, (1996), 289.